Crack growth in the through-thickness direction of hydrided thin-wall Zircaloy sheet

Patrick A. Raynaud [a,*], Donald A. Koss [b], Arthur T. Motta [c]

[a] US Nuclear Regulatory Commission, Washington, DC 20555, USA
[b] Department of Materials Science and Engineering, Penn State University, University Park, PA 16802, USA
[c] Department of Mechanical and Nuclear Engineering, Penn State University, University Park, PA 16802, USA

ARTICLE INFO

ABSTRACT

In a reactivity-initiated accident, cladding failure may occur by crack initiation within a defect such as a hydride rim or blister and subsequent crack propagation through the thickness of the thin-wall cladding. In such a circumstance, determining the cladding resistance to crack propagation in the through-thickness direction is crucial to predicting cladding failure. To address this issue, through-thickness crack propagation in hydrided Zircaloy-4 sheet was analyzed at 25 °C, 300 °C, and 375 °C. At 25 °C, the fracture toughness decreased with increasing hydrogen content and with an increasing fraction of radial hydrides. Hydride particles fractured ahead of the crack tip, creating a path for crack growth. At both 300 °C and 375 °C, the resistance to crack-growth initiation was sufficiently high that crack extension was often caused by crack-tip blunting. There was no evidence of hydride particles fracturing near the crack tip, and no significant effect of hydrogen content on fracture toughness was observed at these elevated temperatures.

Published by Elsevier B.V.

1. Introduction

During operation in a light-water nuclear reactor, zirconium-based nuclear fuel cladding is subject to oxidation by the coolant water, which in turn results in hydrogen ingress into the metal. Unlike radiation damage, hydrogen ingress does not saturate with time, thus becoming a critical issue for high-burnup fuel [1,2]. The cladding thermal gradient caused by the outward heat flow from the fuel into the coolant causes the hydrogen solid solubility limit to be exceeded first in the coolest regions of the cladding tube, near the outer surface. Consequently, after long fuel exposures, a dense region of hydrides called a 'hydride rim' often precipitates near the outer surface of the cladding. Furthermore, thick oxide layers (>80 μm), exhibit an increased incidence of oxide spallation which causes a 'cold spot' in the spalled region because the substrate material is more efficiently cooled. This phenomenon can result in the formation of a lens-shaped solid hydride 'blister' in that location [3]. These hydride rim or blisters in the cladding represent preferential sites for crack initiation on the outer surface of the cladding. In the early stages of deformation during in a postulated reactivity initiated accident (RIA), an axial crack can initiate in the rim or blister, which can lead to failure if such crack can propagate through the thickness of the cladding tube. Thus, the prediction of through-thickness crack growth behavior of cladding material with

a hydride rim or blister is of great importance for the assessment of cladding safety at high-burnup operation [3–5]. In turn, in order to predict cladding failure due to crack growth, the fracture toughness of hydride cladding must be known for the relevant crack growth geometry and for the appropriate hydride and temperature conditions. This study examines the fracture toughness for through-thickness crack growth in thin-wall Zircaloy-4 sheet as a function of hydrogen content and hydride orientation, at temperatures from 25 °C to 375 °C.

Despite the large number of fracture toughness studies on cladding materials, few studies have focused on the combination of conditions mentioned above. Earlier studies examined the toughness of thick plate Zircaloy-2 and Zr–2.5Nb [6–13], or, more recently, that of Zircaloy-4 [14–22]. The effects of hydrogen content, hydride orientation, or of a combination of both, have been studied in some detail for a range of hydride microstructures relevant to the nuclear industry. However, although many crack orientations have been studied, most investigations have focused on axial crack growth in cladding tube, as opposed to through-thickness crack growth. In fact, to the authors' knowledge only Honda [9] and Walker [23,24] have investigated the growth of cracks with an orientation akin to that of through-thickness crack growth in thin-wall cladding tubes. However, both studies used thick plate or thick tube specimens and only Honda reported testing at a temperature relevant for RIA behavior (300 °C). However, since it is well known that (depending on crack orientation) specimen thickness can significantly influence fracture toughness values [25], it is imperative to

* Corresponding author. Tel.: +1 301 251 7542.
E-mail address: patrick.raynaud@nrc.gov (P.A. Raynaud).

perform testing on thin-wall specimen geometries to predict the failure of high-burnup thin-wall cladding tube under RIA loading conditions. The few studies performed on thin-wall cladding specimens investigated axial crack growth instead of through-thickness crack growth [14,18,20,26].

For this study a new test method was developed in order to obtain the fracture toughness of thin (~0.675 mm) unirradiated Zircaloy-4 sheet such that the results relate to the toughness behavior of an axial crack propagating in the through-thickness direction of a cladding tube. In this method a surface crack is propagated through the sheet thickness during four-point bending as a result of displacement in the short-transverse direction (which corresponds to hoop extension in a cladding tube) [27]. The present study extends previous studies [27–29] and uses an ASTM-recommended fatigue precracking procedure [30] in order to be able to precisely determine the initial crack length. Fatigue pre-cracking also allowed better control of the crack length, particularly with respect to the hydride microstructure near the crack tip. Real-time crack length monitoring allowed *J–R* curves to be generated, and quantitative metallographic methods were developed to characterize the local hydride microstructures near the crack tip. Finally, testing was performed at temperatures up to 375 °C, so that the temperature dependence of the fracture toughness for through-thickness crack growth within thin-wall Zircaloy-4 samples was examined as a function of hydrogen content and hydride orientation.

2. Experimental and analytical procedures

2.1. Materials

Cold worked Zircaloy-4 sheet with a thickness of 675 μm was provided by Teledyne Wah-Chang. The as-received sheet was subsequently stress-relieved for 2 h at 520 °C under vacuum of 10^{-3} Pa, resulting in a cold-worked-stress-relieved (CWSR) state. The microstructure of the CWSR Zircaloy-4 sheet was characterized by slightly flattened grains oriented parallel to the plane of the sheet, and elongated in the rolling direction with an average grain size of 6 μm × 4.5 μm × 2.5 μm. The crystallographic texture of the CWSR sheet was similar to that observed in other studies performed on CWSR sheet Zircaloy-4 and on CWSR cladding tube [31]. Pole figures indicated that the average orientation of the basal poles was tilted about 30° away from the normal direction in the transverse direction, and that one of the prism pole directions was aligned with the rolling direction, as expected. The Kearns parameters [32] (the resolved fractions of basal poles aligned with each macroscopic direction) obtained using both the direct pole figure method and the inverse pole figure method [33] are shown in Table 1 and compared to those measured in Zircaloy-4 sheet [34] and in Zircaloy-4 cladding tube [35]. The calculated Kearns factors were in good agreement with previously reported measurements in tubing, confirming the similarity in crystallographic texture between the Zircaloy-4 sheet used in this study and Zircaloy-4 cladding tube.

Tensile testing was performed at 25 °C, 300 °C, and 375 °C in the transverse orientation of the sheet in order to characterize the deformation behavior of the material. The results are summarized in Table 2. The strength of the material in this study was 5–10% lower than that of cladding tube. The strain-hardening exponent is also significantly lower than that of unirradiated cladding, but similar to that of irradiated cladding tube ($n \sim 0.015$) [36]. The plastic anisotropy ratios for both the sheet and cladding tube indicate that these materials are resistant to through-thickness deformation, more so for sheet than for tube. It is believed that the combination of lower strain hardening and higher plastic anisotropy may yield somewhat lower fracture toughness values for the sheet material than for the unirradiated cladding tube. However, it should be pointed out that, within the ranges of parameters covered in this study, the effects of the differences in mechanical properties described here are believed to be small compared to the effects of hydrogen and temperature on the fracture toughness of hydrided Zircaloy-4.

2.2. Fracture toughness testing

To perform the fracture toughness tests, a 'starter' crack of known depth was created using a controlled hydriding procedure that created a linear blister of defined depth extending across the specimen width; see Refs. [27–29]. The linear blister was formed by gaseous hydrogen charging at 370–400 °C in a [12.5% H_2, balance Ar] atmosphere at ~60–65 kPa for 20–60 min. This procedure created a solid linear hydride (called a linear hydride blister) with discrete hydride particles in the base metal underneath. The specimens were subsequently annealed at 400 °C and slow-cooled to coarsen the underlying hydride microstructure. The hydride microstructure thus produced within the Zircaloy-4 substrate was similar to that observed in high-burnup cladding.

Pre-loading of each hydrided test specimen in 4-point bending to less than the yield load resulted in cracking the hydride blister, thus injecting a sharp surface crack extending across the width of the test specimens, as verified by optical measurements and by acoustic emission monitoring [34]. The crack was then grown by cyclically loading the specimen according to ASTM specifications [30] to obtain a fatigue pre-crack that was clearly distinguishable on the eventual fracture surface. This allowed for precise knowledge of the initial crack length.

In order to analyze the crack growth behavior in terms of the load–displacement record during a fracture toughness test, the electrical potential drop (EPD) method was used to determine crack advance through the thickness of the thin-sheet Zircaloy-4 bend specimens. By monitoring the potential drop across the crack, the normalized crack length *a/W* (where *a* is the crack length and *W* the specimen thickness) can be determined using Johnson's equation [37], as described previously for the present specimen geometry [27].

Table 1
Calculated Kearns parameters for Zircaloy-4 sheet material used in this study, compared with previous studies.

Direction	Normal/radial	Transverse/circumferential	Rolling/axial
Present study CWSR sheet			
Direct pole figure method	0.59	0.29	0.12
Inverse pole figure method	0.59	0.31	0.16
Previous studies			
CWSR sheet [34]	0.59	0.31	0.05
CWSR tube [35]	0.58	0.32	0.10

Table 2
Deformation behavior of CWSR Zircaloy-4 in the transverse or hoop direction. In this table, $\sigma_{0.2\%}$ is the yield stress, $n = d(\ln \varepsilon)/d(\ln \sigma)$ is the strain-hardening exponent, and $P = (\varepsilon_{width}/\varepsilon_{thickness})^{transverse}$ is the plastic anisotropy factor.

	$\sigma_{0.2\%}$ (MPa)	n	ε_f (%)	P
25 °C				
CWSR sheet (this study)	575	0.018	17	2.6
Unirradiated CWSR cladding tube [31]	590	0.068	NA	1.3
300 °C				
CWSR sheet (this study)	315	0.032	20	1.9
Unirradiated CWSR cladding tube [31]	350	0.059	NA	1.5
375 °C				
CWSR sheet (this study)	290	0.027	22	1.6

After fracture toughness testing, the remaining ligament of each fracture toughness specimens was broken to expose the fracture surfaces, and a measuring microscope was used to determine both the initial fatigue pre-crack length and the final (heat-tinted) crack length at several locations along the crack front before final fracture. The average crack length data were then used to precisely calibrate the potential drop measurement so that crack extension could be determined during the test before fracture. In addition, since the crack depth was not always uniform across the specimen width, the profiles of the initial and final crack fronts were obtained and used to assess crack uniformity. For cracks with non-uniform crack lengths, FRANC3D software [38] was used to calculate stress intensity factors along the crack front during the test.

Selected specimens were subjected to interrupted-testing to assess crack-front profiles and crack-tip blunting at different levels of crack extension. These specimens were sequentially tested at incremental degrees of crack extension, and a thin-strip section was removed along their length after each increment of crack growth and load–displacement. This procedure permitted observations of the crack tip profile at different stages of crack extension and crack growth behavior by mounting the strips removed at various amounts of bending for metallography and back-scattered scanning electron microscopy (SEM) observation.

2.3. Hydride microstructure characterization

The hydride orientation was characterized as a function of depth in the sheet specimens to assess its influence on fracture toughness. For the hydriding procedure used, the hydride orientation varied through the thickness. The region directly beneath the blister generally contained 'radial' hydrides (i.e., oriented normal to the plane of the sheet), while only 'circumferential' hydrides (i.e., parallel to the plane of the sheet) were present far away from the blister. The 'radial' hydride particles emanating from the blister were termed 'sunburst' hydrides, while the region showing hydrides of both orientations beneath the 'sunburst' was termed the 'mixed' hydride region [27]. Image analysis tools were used to quantitatively characterize the hydride microstructure reflected in light microscopy examinations in terms of hydrogen content and radial hydride fraction.

The hydrogen content in the vicinity of the crack tip was estimated by computing the area fraction of hydride particles using Image J freeware [39]. As illustrated in Fig. 1, the images (optical micrographs of etched surfaces) were first enhanced for contrast between metal and hydrides, and then turned into binary images that were filtered to obtain an accurate area fraction measurement. The 'apparent' hydrogen content was then calculated from the area fraction using the following equation [40]:

$$[\text{H}]_{\text{total}} = [\text{H}]_{\delta\text{-ZrH}_x} \cdot F_{\delta\text{-ZrH}_x} \cdot \left[\frac{\rho_{\delta\text{-ZrH}_x}}{\rho_{\alpha\text{-Zr}} \cdot (1 - F_{\delta\text{-ZrH}_x}) + \rho_{\delta\text{-ZrH}_x} \cdot F_{\delta\text{-ZrH}_x}} \right]$$

(1)

where $[\text{H}]_{\text{total}}$ is the total hydrogen content (wt.ppm); $[\text{H}]_{\delta\text{-ZrH}_x}$ is the hydrogen content for the δ-phase of $\text{ZrH}_{\sim1.6}$ which translates to $\sim$17,570 wt.ppm; $\rho_{\delta\text{-ZrH}_x}$ is the density of the δ-phase (equal to $\sim$5.65 g/cm^3 at room temperature); $\rho_{\alpha\text{-Zr}}$ is the density of the α-phase of Zircaloy-4 (equal to $\sim$6.54 g/cm^3) at room temperature; and $F_{\delta\text{-ZrH}_x}$ is the hydride area fraction [41,42]. Because at room temperature the amount of hydrogen in solution in the metal is negligible (less than 5 wt.ppm at equilibrium) [43], no correction was made to account for it.

As might be expected from the chemical etching attack of the metallographic specimen, the 'apparent' hydrogen content from the area fraction of hydrides as given by Image-J procedure overestimates the actual hydrogen content in the specimen. As a result, it was necessary to benchmark the image analysis procedure by comparing area fraction measurements with actual hydrogen contents measured by hot-vacuum extraction [44]. The benchmarking procedure established a "correction factor" that was similar to that observed by others using a similar procedure [41].

In addition to estimating the hydrogen content from area fraction measurements, the radial hydride fraction was computed using the software package Hydromorph, developed by CEA and IRSN [45]. Using Hydromorph, every hydride within a given micrograph is identified, skeletized, and indexed. The results are then used to compute the length and orientation of each indexed hydride [44]. Depending on their orientation, hydrides were classified as 'in-plane' (oriented between 0° and 40° from the plane of the sheet metal), 'mixed' (40–65°), or 'out-of-plane' (65–90° to the plane of the sheet). In order to take into account both the mixed
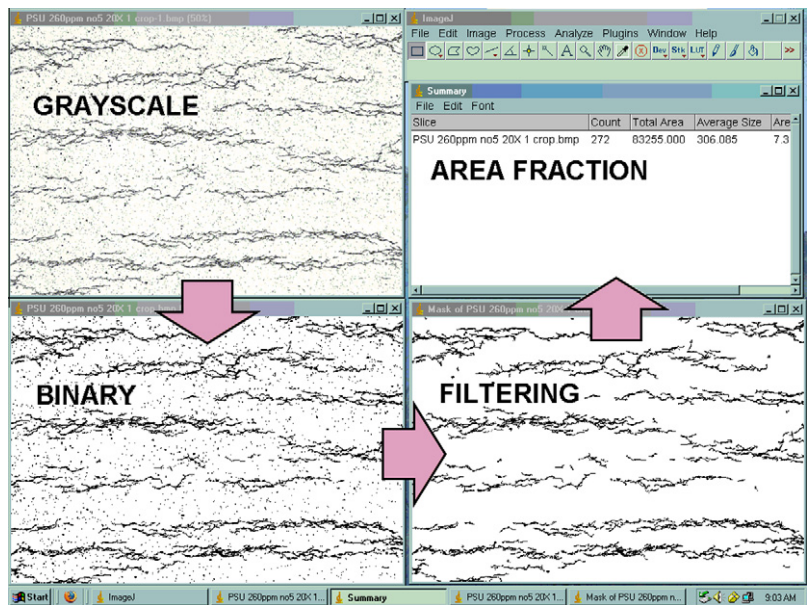

Fig. 1. The sequence of steps for area fraction determination for zirconium hydrides in a Zircaloy-4 metal matrix using Image-J software.

hydride fraction and the out-of-plane hydride fraction, the radial hydride fraction (RHF) was defined by the weighted average given in the following equation:

$$\text{RHF} = \frac{0.5 \cdot \sum_i L_i^{\text{mixed}} + \sum_j L_j^{\text{out-of-plane}}}{L_{\text{total}}} \times 100 \qquad (2)$$

where RHF is the radial hydride fraction; L_i^{mixed} and $L_j^{\text{out-of-plane}}$ are the length of the mixed orientation particle 'i' and the length of the out-of-plane oriented particle 'j', respectively; and L_{total} is the sum of the lengths of all the particles analyzed, regardless of their orientation (in-plane, mixed and out of plane).

As shown in Fig. 2, micrographs of the area underneath the hydride blister were sectioned into 50 μm high bands and analyzed using both Hydromorph and Image-J for each test specimen. It was thus possible to determine the variations in both hydride content and radial hydride fraction through the thickness of test specimens. Knowing the variations of the hydride microstructure through the specimen thickness and the length of the initial crack during fracture toughness tests, it was possible to determine the fracture toughness as a function of the hydride microstructure in the vicinity of the crack tip.

2.4. Fracture mechanics considerations

Because of the significant degree of plasticity observed during fracture toughness testing of the hydrided thin-sheet Zircaloy-4 specimens used in this study, it was necessary to use elastic–plastic fracture mechanics (EPFM) to analyze the test results. In particular, the resistance curve test method described in standard procedure ASTM E1820 [30] provided the necessary guidelines and EPFM data analysis procedures to obtain 'J–R curves', from which the J-integral value at the onset of crack growth was determined. Eq. (3) was used to determine the J-integral value at any given point 'i' of the load–displacement response:

$$J_{\text{tot}}^i = J_{\text{el}}^i + J_{\text{pl}}^i = \frac{K_i^2(1-\nu^2)}{E} + J_{\text{pl}}^i \qquad (3)$$

where J_{tot}^i is the total J-integral, J_{el}^i is the elastic portion of the J-integral, K_i is the elastic stress intensity factor for this configuration, ν and E are Poisson's ratio and Young's modulus, respectively, and the plastic portion of J-integral, J_{pl}^i is given by the following equation:

$$J_{\text{pl}}^i = \left[J_{\text{pl}}^{i-1} + \left(\frac{\eta_{\text{pl}}^i}{b_i} \right) \left(\frac{A_{\text{pl}}^i - A_{\text{pl}}^{i-1}}{B} \right) \right] \left[1 - \gamma_{i-1} \frac{a_i - a_{i-1}}{b_{i-1}} \right] \qquad (4)$$

where W is the specimen thickness, a_i is the crack length, $b_i = W - a_i$, is the length of the remaining ligament, B is the specimen width, and A_{pl}^i is the amount of plastic energy spent by the applied load up to crack increment 'i' (the plastic energy under the load–displacement curve). The terms η_{pl} and γ are geometric factors directly related to each other and which depend on crack length [46]. The fracture toughness K_J^i derived from the J-integral for plane strain calculated at point 'i' is given by the following equation:

$$K_J^i = \sqrt{\frac{J_{\text{tot}}^i}{(1-\nu^2)}} \qquad (5)$$

Based on the procedures described in ASTM E1820 [30], J–R curves were used as a means of obtaining the fracture toughness at the onset of crack growth, and the following three values of J-integral were identified:

- The intersection of the J–R curve and the blunting line (corresponding to the initiation of stable crack growth) was termed J_i (analogous to $J_{0.2\text{mm}}$ in ASTM standard terminology).
- When unstable crack growth occurred, the J-integral value at the onset of unstable crack growth was termed J_c.
- Finally, the value of the J-integral at the point of maximum load in the load–displacement curve was termed $K_{JP\text{max}}$.

Given the geometry of the specimens used in this study, some of the requirements defined in ASTM E1820 [30] could not be fulfilled. In particular, the small thickness (∼0.6 mm) of the sheet Zircaloy-4 used in this study to emulate the behavior of cladding tube did not permit the standard specimen geometry ratios to be used. For example, the width of a typical sheet specimen was generally larger than 10 times its thickness, instead of the 0.25–1 times the thickness specified by ASTM E 1820. In the present case, the large specimen width dictated a predominantly plane-strain condition along the crack front, despite the thin-sheet specimen geometry.

The small thickness of the sheet Zircaloy-4 specimens also rendered inapplicable the 0.2 mm blunting line offset (in the load–displacement data) for crack growth initiation specified by ASTM E1820. For a physically large ASTM specimen, the 0.2 mm offset represents only a small fraction of the crack extension ex-
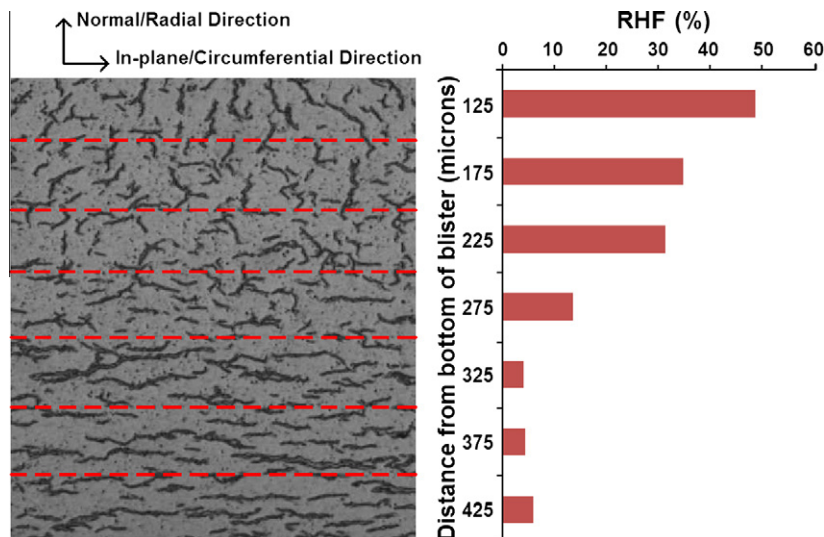

Fig. 2. Example of radial hydride fraction (RHF) measurement through the thickness of a sheet Zircaloy-4 specimen. The calculated hydrogen content is in this sample [H] ∼ 240 ± 30 wt.ppm.

pected to occur during a test. However, in the present study for specimens ~0.6 mm thick, the total crack extension was often smaller than $\Delta a = 0.2$ mm. Thus in order to identify when crack extension had an identifiable crack growth increment in the J–R data, the following procedure was used to establish a blunting line offset for our specimen geometry. The procedure relies on characteristics of crack profiles in which multiple through-thickness cracks extended from a hydride blister in Zircaloy sheet under either plane-strain tension [34] or equal-biaxial tension [47]. As shown in Fig. 3, the crack profiles of the arrested cracks provide an image of crack extension prior to unstable crack growth. An examination of several such images [34,48] shows that little crack-tip blunting occurs ($\leqslant 10$ μm) *at room temperature*, implying that crack extension due to blunting should be less than about 5 μm. Importantly, it was observed that when blunted cracks emit a crack, it is at least 10 μm long. Thus, the room temperature J–R curves were analyzed using a blunting line with an offset of 10 μm to establish crack growth initiation.

As shown in Fig. 3b and c, crack-tip profiles at 300 °C show extensive crack-tip blunting that result in crack extension for through-thickness cracking under a plane-strain condition beneath a hydride blister [34,48]. The crack extension caused by the crack-opening displacements is in the range of 35–45 μm for cracks of similar depth to those in this study; see Fig. 3b and c. On the other hand, when crack growth initiation occurs from a blunted crack tip, as is the case in Fig. 3d for equal-biaxial tension at 300 °C [47], the initiated crack has a sharp tip and is larger than 10 μm. The J–R curves at elevated temperature testing were thus also analyzed using a blunting line with an offset of 10 μm to establish crack growth initiation.

In addition to establishing the very small offset for the blunting line, it was necessary to address a non-uniform crack profile issue

for some of the specimens in the analysis of the data for J-values. Because of the thin-wall specimen geometry, small variations of the fatigue pre-crack length across the width of a test specimen could result in significant variations of the (a/W) ratio and therefore of the local stress intensity factor along the crack front. It should be recalled that the electrical potential drop (EPD) method used to monitor crack length is insensitive to the variations of crack length along the crack front and only provides an average crack length. As a result, the J-integral fracture toughness values generated from the EPD record did not always accurately reflect the local stress intensity factor variations along the crack front. To take a non-uniform crack profile into account, the software Franc3D [38] was used to model the effects of a locally varying crack length on the stress intensity factor along the crack front. The actual geometry of the crack front, as measured on the fracture surfaces after J-testing was used in the Franc3D calculation. In particular, the software was used to compare the local stress-intensity factor along the uneven crack front to that of a straight crack of average length.

The Franc3D model was used to analyze those specimens (a minority) in which the local crack length deviated from the average crack length by more than 10% of the specimen thickness (i.e., $a/W > 0.10$). The average crack length was calculated by integrating the crack length along the crack front, and two separate models of the same cracked thin-sheet specimen were created under Franc3D. The first model contained a uniform straight crack of depth equal to the average crack length, while the second model was generated using the actual crack profile. The computations of the stress intensity factors K_I along the crack front were obtained from the first model (containing the uniform crack front) and compared to those obtained from the second model (containing the non-uniform crack front) by calculating the ratio K_I (actual crack)/K_I(straight crack).
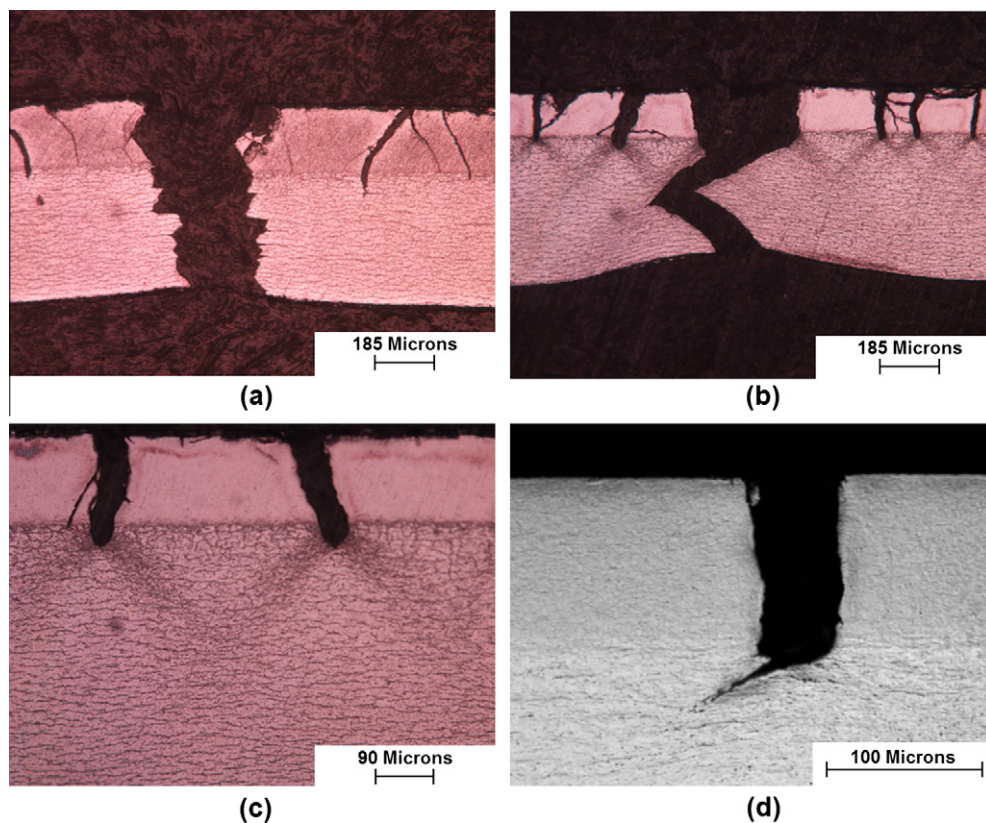

Fig. 3. Fracture profiles of CWSR Zircaloy sheet fractured (a) at room temperature under plane-strain tension, (b and c) at 300 °C also under plane-strain tension, and (d) at 300 °C but under equal-biaxial tension. In all cases, the cracks initiated within the hydride blister in the upper section of the image. Figures (a–c) are after [34,48], and (d) after [47].
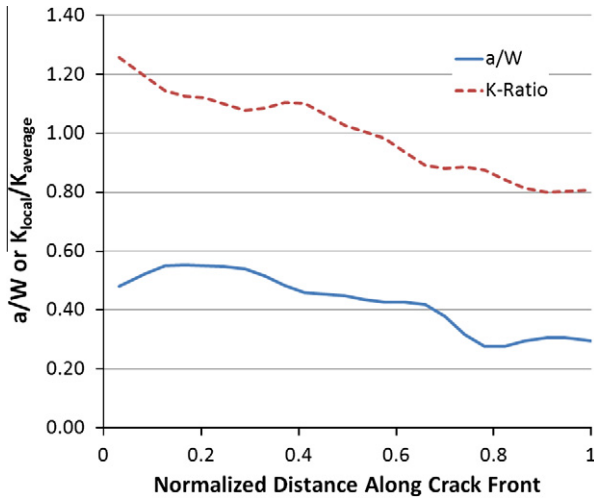
Fig. 4. Normalized stress-intensity factor along the crack profile for a non-uniform crack, and the crack length profile (*a/W*) of the corresponding crack.

As an example, Fig. 4 depicts the results of a Franc3D calculation in which an extremely non-uniform crack with *a/W* ranging from ~0.25 to ~0.50 was modeled for a cracked thin-sheet specimen subjected to uniform bending at 25 °C. Despite the bending mode of loading, Fig. 4 shows that the lowest value of the calculated stress intensity factor occurred where the crack was the shallowest and increased gradually to where the crack was the deepest. In this specific case, the local stress intensity factor varied between 80% and 125% of the average stress intensity factor. As will be discussed later, for reasons related to hydride microstructure, the crack advanced initially along the crack front region with shortest crack depth. Consequently, in order to obtain the fracture toughness at the onset of crack growth for this example, the fracture toughness at the onset of crack growth obtained from the *J–R* curve for a crack of *average* length was multiplied by a factor of 0.8 in order to account for crack growth initiation along the "short crack" segment.

3. Results and discussion

3.1. Load–displacement and crack-growth behavior

The crack growth behavior varied considerably over the range of test temperatures and in response to the hydride microstructures at the crack tip. As shown in Fig. 5, significant differences were observed between the load–displacement behavior during testing at 25 °C and at high temperature (300 °C and 375 °C). At 25 °C, the load–displacement curve exhibited a well-defined maximum-load point, followed by either a sharp load drop at constant displacement if *unstable* crack growth occurred, or a gradual loss of

load if stable crack growth occurred; Fig. 5a. As shown, little crack extension takes place prior to maximum load. Furthermore, the load decrease observed at 25 °C after maximum load was associated with significant crack growth, and the extent of crack growth was roughly proportional to the increment of load loss.

In contrast, the load–displacement curves at 300 °C and 375 °C (which were quite similar in appearance), were characterized by a gradual approach to maximum load. As depicted in Fig. 5b, this near-plateau in load was followed by a gradual load loss associated with extensive plastic deformation in the specimen. In such a circumstance, the maximum load is not especially significant with regard to fracture toughness, because (i) its location is difficult to determine with precision, which could lead to significant uncertainties in the determination of the toughness-value, and (ii) while the gradual load loss is caused primarily by crack extension, it is unknown whether the extension is due to crack growth initiation or to crack-tip blunting.

Fig. 6 shows crack-tip profiles obtained from a sequence of interrupted testing. Fig. 6a and c depicts crack growth behavior at 25 °C, which is characterized by growth of a relatively sharp crack. This growth happens initially through the 'sunburst' and 'mixed' hydride regions, where the crack plane and crack-growth direction are parallel to some of the hydride particles. The crack tip remains relatively sharp upon entering the field of in-plane hydrides but blunts and branches due to the fractured in-plane hydride particles in its path. Subsequent crack advance occurs by a damage accumulation process in which large hydride particles fracture ahead of the crack tip, and the crack tip subsequently links to the hydride-induced void ahead of it by micro-void nucleation, growth and coalescence (Fig. 6c).

Fig. 6b and d shows the contrast in crack profiles between room temperature and elevated temperature. As is evident in Fig. 6b, initial crack extension at 300 °C (just beneath the hydride blister in this example) is associated with extensive crack-tip blunting, which is consistent with the behavior of hydrided Zircaloy-4 during high temperature testing seen previously [34,47,48] (examples of which were shown in Fig. 3). After continued loading and extensive bending (at which the specimen had bent to an angle of nearly 50°), Fig. 6d shows a blunted crack with an irregular profile such as might occur due to either tensile fracture at a notch or an increment of crack growth accompanied by significant crack blunting. We note that, within the range of hydride microstructures tested, there appeared to be little direct influence of the hydride particles on crack growth at 300 °C and 375 °C. For example, no hydride-induced voids were observed near the crack tip at either 300 °C or 375 °C as shown in Fig. 6c.

Temperature had a significant effect on the shape of the crack front across the width of the specimens as crack extension occurred. As shown in Fig. 7a, despite an initial non-uniform crack front geometry induced by fatigue in some tests, the final crack front after tensile crack growth under quasi-static loading at
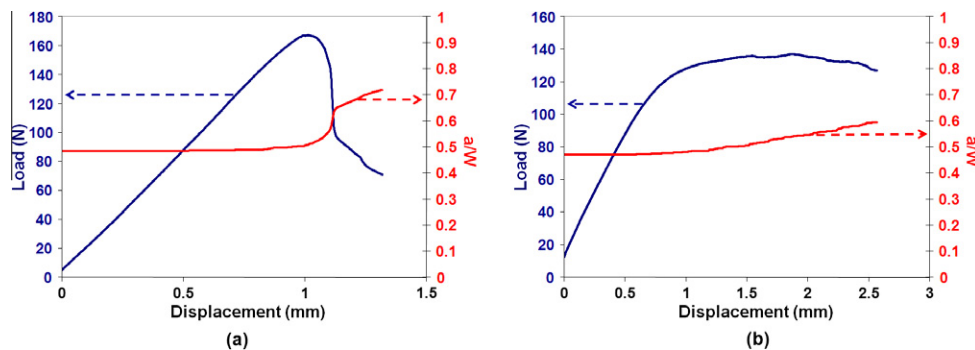

Fig. 5. The load–displacement response correlated with crack length at (a) 25 °C and (b) 300 °C.
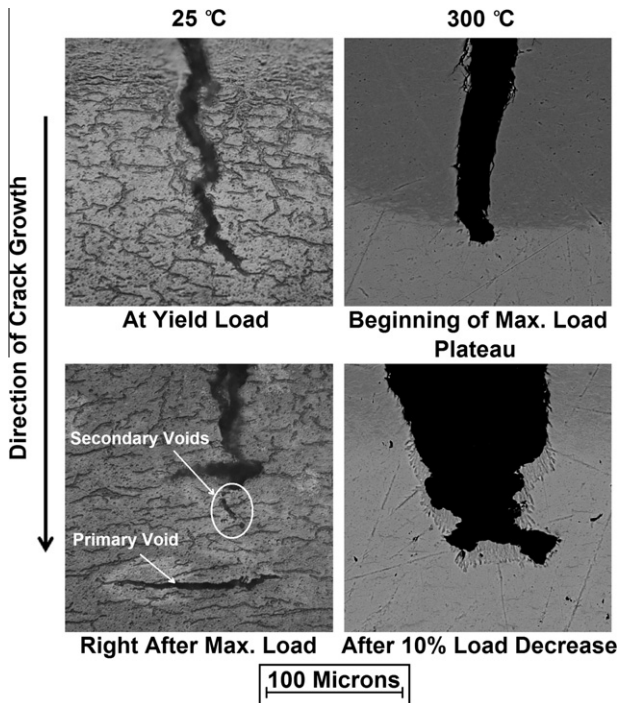
Fig. 6. Crack tip profile evolution with increasing amounts of specimen displacement (top to bottom) of the fracture toughness test specimens at 25 °C and 300 °C. All images are shown at the same magnification.

25 °C was always relatively straight and uniform in length. Thus, through-thickness crack growth at room temperature occurred in a manner that resulted in uniform crack length. Such a straight final crack profile implies that in those tests crack growth at 25 °C occurred first where the crack was most shallow (i.e., smallest a/W). Although counter intuitive (since the stress intensity factor is highest in the deeper crack region), this crack-growth behavior may be explained by the different hydride microstructure seen in the region where the shallow crack is propagating. At small crack lengths, the crack-tip advance was likely in a region within the specimen thickness where the hydride particles are frequently in the 'out-of-plane' orientation and therefore oriented co-planar with the crack plane; see Figs. 2 and 6a. Thus, crack growth initiation occurs at locations along the crack front with a high proportion of out-of-plane hydrides, implying a locally lower fracture toughness, as would be expected [27,29]. A quantitative correlation between fracture toughness and hydride orientation will be presented later in this study.

In contrast with the behavior at 25 °C, the final crack front at 300 °C and 375 °C had the same overall shape as the initial crack front (i.e., the crack front did not straighten out during deformation), as shown in Fig. 7b. This indicates that at high temperatures (300 °C and 375 °C), crack extension occurred uniformly all along the crack front, despite differences in the crack front proximity to the hydride blister. Since the hydride particle microstructure varied within the thickness of these specimens, this behavior implies that the discrete hydride particles likely had little influence on the crack growth process at or above 300 °C. [It should be noted that the hydrogen solubility in Zircaloy-4 is 70 wt.ppm and 150 wt.ppm at 300 °C and 375 °C, respectively [41]. As estimated from metallography near the crack tips, the hydrogen contents of all but one of the specimens tested would still have at least some hydride particles within the Zircaloy-4 matrix.]

The influence of temperature on the crack-tip fracture process is also apparent in the associated fractography. Fig. 8 shows tensile fracture surfaces obtained by SEM fractography, for specimens tested at 25 °C, 300 °C and 375 °C. At 25 °C, the cracking of large elongated hydride precipitates in the Zircaloy-4 matrix formed large primary voids in the plane of the sheet specimen (Fig. 8a) with lengths that varied between 20 μm and 300 μm. In addition, small secondary equiaxed dimples are visible in Fig. 8a. These dimples likely resulted from void nucleation ahead of the crack tip during the crack growth process that links the crack tip to the next primary void ahead of it, as shown in Fig. 6a and c. The formation of a number of very large hydride-initiated primary voids, in conjunction with the crack propagating by linkage of these large voids, caused the fracture surface to appear quite rough and irregular.

As seen in Fig. 8b and c, the fracture surfaces created during toughness testing at 300 °C and 375 °C were significantly different from those observed at 25 °C. At 300 °C and 375 °C, despite much larger plastic strains than at room temperature, large elongated primary voids were not present in the fracture surface. Instead, as shown in Fig. 8b, at 300 °C there was evidence that elongated particles failed with a certain amount of ductility, forming 'ridges' on the fracture surfaces. The absence of large hydride-induced primary voids and the presence of ductile elongated ridge features strongly suggests ductile behavior of the hydrides at these temperatures, as also observed by Glendening et al. [47] and Bertolino et al. [15,17] in their studies of the fracture of hydrided Zircaloy-4 at 300 °C. At 375 °C, these elongated features associated with the hydride particles were not observed, likely because a larger proportion of the hydride particles were dissolved into the matrix at that temperature. In this case, the fracture surfaces were characterized by a distribution of equiaxed micro-void 'dimples'.

In summary, these observations indicate that hydride particles directly contribute to the initiation and growth of through-thick-
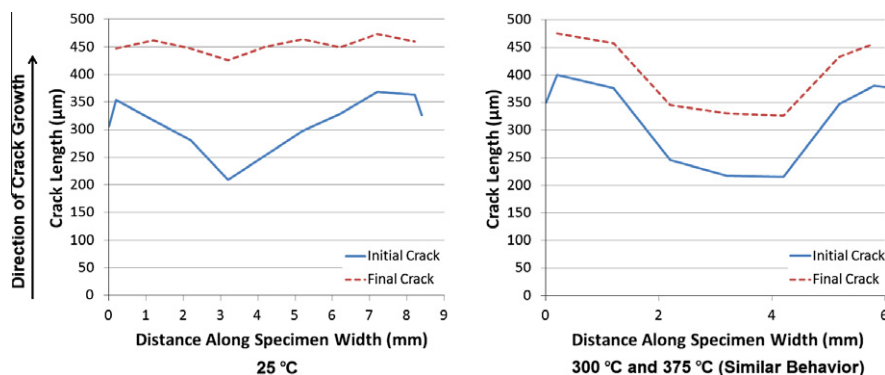

Fig. 7. Typical crack front profiles observed in this study at room temperature (25 °C) and at high temperature (300 °C and 375 °C). The example shown was obtained at 300 °C.
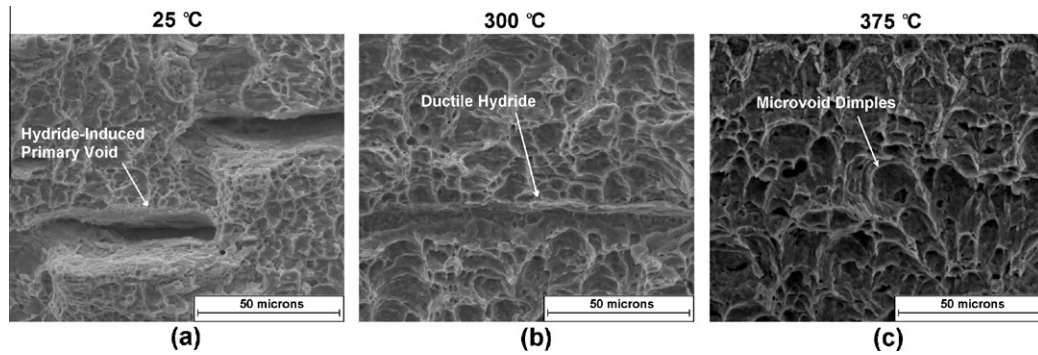
Fig. 8. Scanning electron micrographs showing the fracture surfaces obtained from toughness testing at (a) 25 °C, (b) 300 °C, and (c) 375 °C.

ness cracks at 25 °C. However, the resistance of hydride particles to damage initiation at 300 °C and 375 °C and the pronounced crack-tip blunting behavior at these temperatures suggests that hydrides have little influence on the fracture toughness at these elevated temperatures. This is borne out by the calculations of fracture toughness presented in the next section.

3.2. Fracture toughness: the η_{pl} parameter

In order to obtain fracture toughness values, load–displacement and crack extension data such as in Fig. 5 had to be analyzed in the manner of ASTM E1820. However, the small specimen thickness of the thin-sheet specimens raised an important issue in adapting the ASTM E1820 analysis to the present case. Namely, the geometry factor η_{pl}, which is a critical parameter in Eq. (4) to calculate the plastic component J_{pl} of the J-integral, had to be re-calculated for through-thickness crack growth in our non-standard thin-sheet geometry. Previous studies [49–51] have examined η_{pl} values as a function of normalized crack length (a/W) for the case of thick plates containing a crack. In this study, the finite element code Cast3M [52] was used to examine η_{pl} for our thin-sheet single-edge four-point bend geometry.

Fig. 9 shows the mesh used for the determination of the η_{pl} values for the thin-sheet geometry, with a detailed view for the case where the crack length is $a = 100$ μm. The type of element used to create the mesh was a combination of second-order 8-node quadrangles and 6-node triangles. Only half of the specimen and the halves of the loading pins that were in contact with the specimen were modeled in 2D for plane-strain conditions. Horizontal displacements were prevented for the nodes constituting the un-

cracked ligament to account for symmetry. Frictionless contacts were imposed between the loading pins and the specimen, and displacements were prevented for the outer loading pin, while the inner loading pin was only allowed to move vertically upwards to simulate bending. The loading pins were modeled as hardened steel and were considered perfectly elastic. The specimen was modeled using the elastic–plastic properties of cold-worked stress relieved (CWSR) Zircaloy-4 at 25 °C, as determined by tensile tests performed in this study (see Table 2). Anisotropy was not taken into consideration in the model, and the Zircaloy-4 constitutive equation used is given by:

$$\begin{cases} \sigma = E\varepsilon, & \sigma < \sigma_y \\ \sigma = K\varepsilon_p^n, & \sigma > \sigma_y \end{cases}$$

with $E = 99.3$ GPa, $K = 647$ MPa, $n = 0.018$, and $\sigma_y = 575$ MPa.

The code was first benchmarked by reproducing results published in a paper by Kim for cracked plates with ASTM E1820 4-point bend geometries, where the ratio of the distance L between the center loading pins over the thickness W of the specimen is $L/W = 2$ [49], and then used to model the thin-sheet geometry tested in this study. Fig. 10 shows a comparison between Kim's published results [49] (black line), the η_{pl} values found using Cast3M for the thick-plate ASTM geometry (squares) and the thin-sheet geometry (lozenges) tested in this study. As seen in Fig. 10, there is overall good agreement (i.e., within 15% for $a/W < 0.4$ and 5% for $a/W > 0.4$) between Kim's results and those obtained using Cast3M for thick-plate geometries, thus validating the finite element model developed for this study. The small differences observed could be due to differences in the numerical code,
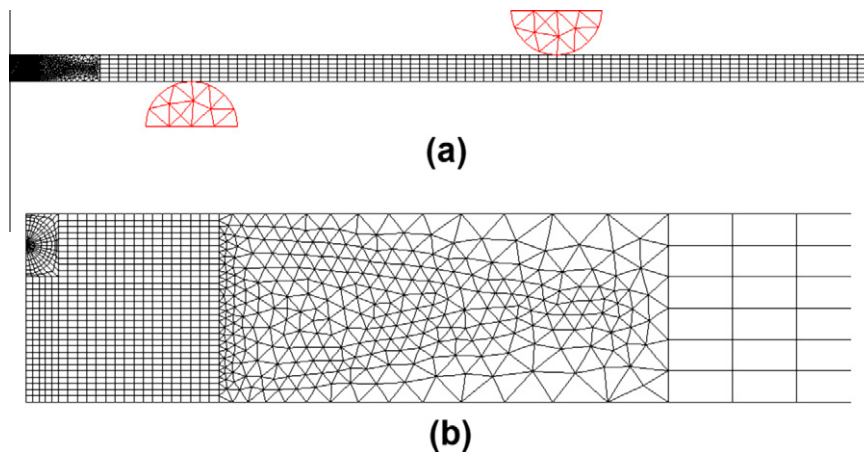

Fig. 9. (a) Finite element mesh used in the Cast3M code to calculate the η_{pl} parameter and (b) close-up of the crack region for a 100 μm crack.
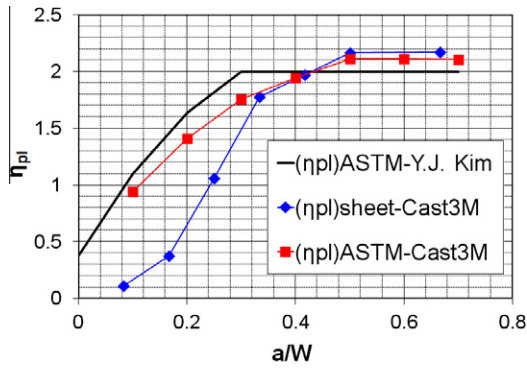
Fig. 10. The predicted values of the η_{pl} parameter as a function of the normalized crack length a/W for a thick-plate ASTM geometry and through-thickness crack growth in a thin-sheet geometry. The η_{pl} parameter predicted by Kim is shown for comparison [49].

mesh design, boundary conditions, numerical scheme utilized to computed the J-integral, and precise method used to calculate η, as mentioned by Davies et al. in their review of η calculation studies [53].

Once the Cast3M code was validated by reproducing Kim's published results [49], the finite element software was used to create a model of the thin sheet specimen containing a through-thickness crack used in this study, for which $L \approx 13W$. In contrast with the ASTM thick-plate case, while the η_{pl} values for thin-sheet and thick-plate are similar in the a/W region from 0.35 to 0.8, they are markedly different in the range $a/W \leqslant 0.35$. As shown in Fig. 10, the thin-sheet η_{pl} value for $a/W \leqslant 0.35$ is significantly lower than that for thick-plate geometry. Thus, care must be exercised in analyzing elastic–plastic through-thickness crack growth behavior for thin sheet configurations with short cracks of $a/W \leqslant 0.35$.

The deviation of the η_{pl} parameter from a constant value of 2 at low a/W values has been addressed by Davies et al. who suggested that this phenomenon is due to the occurrence of more plastic deformation in the bulk away from the crack tip [53]. This hypothesis was examined by plotting the equivalent plastic strain on the deformed finite element mesh, as depicted in Figs. 11 and 12 for increasing crack depths for the thick plate and thin sheet geometries, respectively. As is evident in these two figures, plastic deformation is distributed more in the bulk of the specimen for short cracks, while it concentrates near the crack tip at larger a/W ratios, hence corroborating Davies et al.'s hypothesis.

In addition, Fig. 10 shows that at small a/W ratios, the deviation of the η_{pl} parameter from a constant value of 2 is much larger for a thin-sheet specimen than for a thick-plate specimen. This observation is consistent with the predictions made by Davies et al. [53] concerning the influence of the specimen geometry on η_{pl}, and in particular the influence of the ratio L/W (the ratio of the distance between the center loading pins to the thickness of the specimen). Davies et al. predicted that η_{pl} decreases significantly for short cracks with increasing L/W (as is the case for the sheet geometry); this effect is caused by more extensive plastic deformation in the bulk material away from the crack tip. In the present study for thin-sheet specimens with small a/W ratios, the volume of plastically deformed material (V) is comprised of most of the specimen located between the center loading pins (Fig. 12a). This volume is equal to $V_{\text{sheet}} = BLW \approx 13BW^2$ (with B the width of the specimen, L the inner loading-pin span, and W the thickness of the specimen). In the case of the thick plate (Fig. 11a), the corresponding plastically deforming volume is equal to $V_{\text{plate}} = BLW \approx 2BW^2$. This large difference in the volume of material experiencing plastic deformation (at roughly similar levels of deformation) is likely the cause of the small η_{pl}-values for thin-sheet specimens at small a/W ratios (Fig. 10).
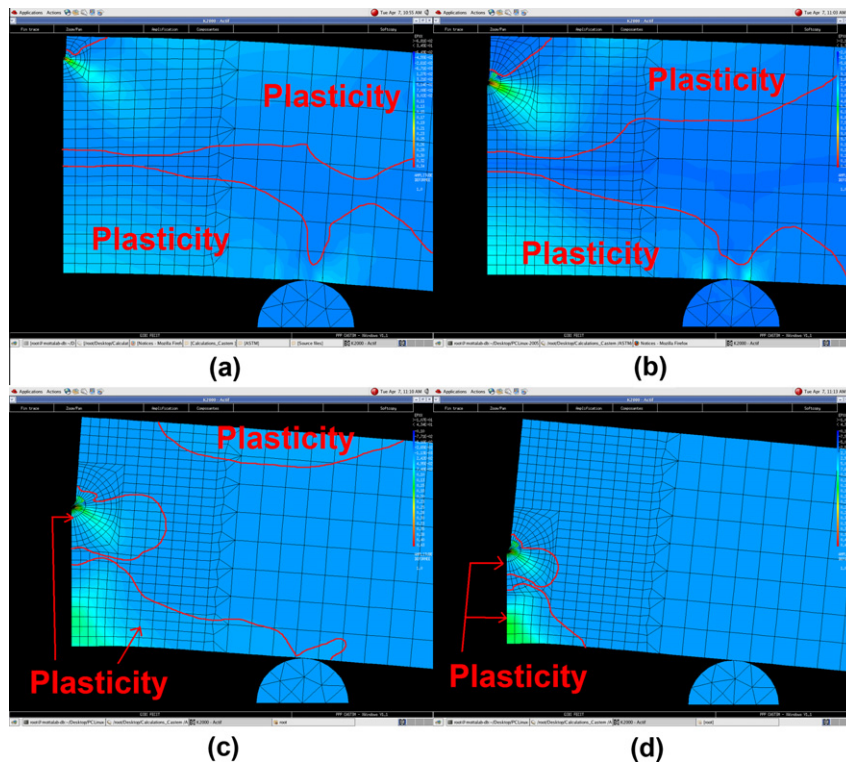

Fig. 11. (a–d) Thick-plate ASTM geometry: equivalent plastic strain distributions at similar bending increments for a/W = 0.1, 0.2, 0.4, and 0.6, respectively. The plastically deformed areas are highlighted.
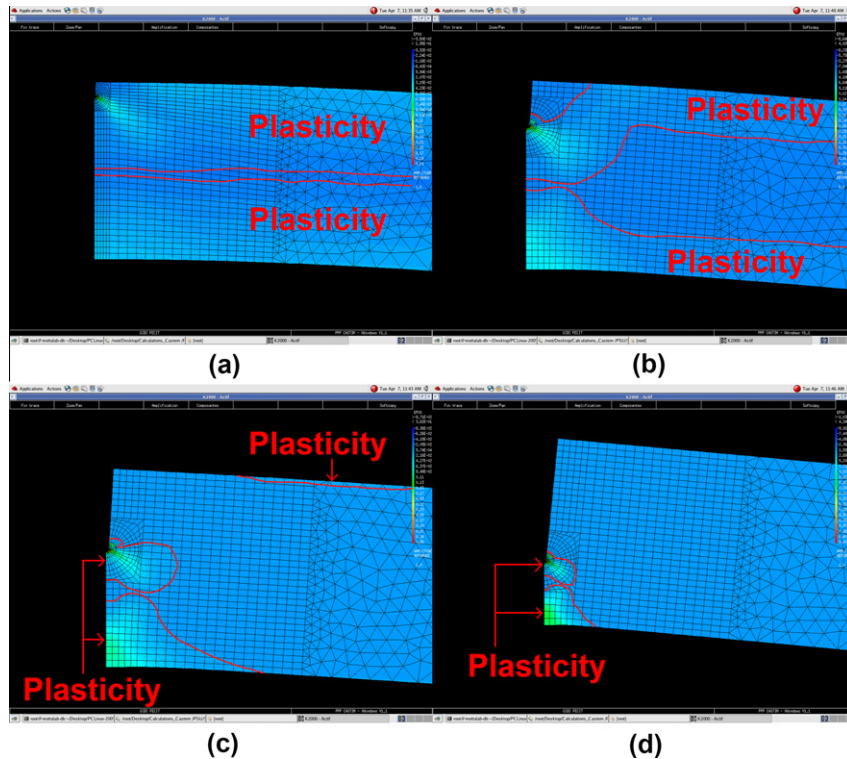
Fig. 12. (a–d) Thin-sheet geometry: equivalent plastic strain at similar bending increments for a/W = 0.08, 0.25, 0.42, and 0.67, respectively. The plastically deformed areas are highlighted.

3.3. Fracture toughness: the J–R behavior

Based on load–displacement records and electrical potential drop (EPD) measurements of crack lengths, $J–R$ resistance curves were generated for the hydrided Zircaloy-4 sheet specimens under conditions of through-thickness crack growth, and these are shown in Fig. 13. As discussed previously, a blunting line offset of 10 μm was chosen to establish crack growth initiation, so in Fig. 13 a solid line with a slope equal to $2\sigma_y$ is shown to indicate crack extension due to blunting while the dotted line indicates the 10 μm offset. As illustrated in Fig. 13a and b two distinct load–displacement behaviors were observed at 25 °C. In some specimens unstable crack growth occurred, in which the abrupt load drop accompanying crack growth caused a discontinuity in the $J–R$ curve. Consequently, the J-integral at the onset of unstable crack growth (termed 'J_c') was used to define the through-thickness fracture toughness of these specimens, as shown in Fig. 13a. Other specimens tested at 25 °C did not exhibit unstable crack growth. In those cases failure was defined as the onset of *stable* crack growth, and thus the intersection of the $J–R$ curve with the blunting line (termed 'J_i') was used to define the through-thickness fracture toughness of the thin-sheet Zircaloy-4, as shown in Fig. 13b. The incidence of the instability discussed above was not related to hydrogen content or radial hydride fraction, but appeared to be more closely related to the amount of stored energy in the sample, which is higher in the samples with short initial crack depths.

At elevated temperatures, two distinct types of $J–R$ responses were also observed. At 300 °C, roughly half of the $J–R$ curves were nearly linear and close to the construction line that indicates crack extension due to crack-tip blunting, as shown in Fig. 13c. The other half of the specimens tested at 300 °C exhibited significant deviations from the blunting line, as illustrated in Fig. 13d. At 375 °C, the nearly linear $J–R$ responses dominated the material behavior; see Fig. 13e. Importantly at both of these temperatures, the slope of the linear portion of the $J–R$ curve is that expected ($\approx 2\sigma_y$, where

σ_y is the yield stress at temperature) when crack extension is due to crack-tip blunting. This behavior persisted even though the $J–R$ data were obtained to displacements well past maximum load (usually to where the load had decreased at least 10%) by which time the specimens were bent to an angle of $\approx 50°$ (where 0° represents a flat specimen).

In contrast to the above, in half of the tests at 300 °C and in one test at 375 °C, the $J–R$ response differed significantly from that described above. In these cases, the $J–R$ curves displayed behavior consistent with crack growth initiation that occurred after a short period of crack extension due to blunting; an example of this type of $J–R$ response is shown in Fig. 13d. For these cases, a J_i-value was determined using the 10 μm blunting line offset, although the nature of the data imply a significant level of experimental scatter in most of the resulting J_i-values, as illustrated in Fig. 16 presented below.

The reason for the different $J–R$ behaviors observed is not known. No correlation was observed between particular types of $J–R$ behavior and microstructural characteristics such as hydrogen content, radial hydride fraction or initial blister size, but since these characteristics were determined post facto, and only for a representative region of the sample it is possible that undetected variations in these parameters can account for the differences in $J–R$ behavior. Crack extension due to extensive crack blunting at elevated temperatures is consistent with the previously observed behavior of cracks in hydrided Zircaloy-4 sheet under plane-strain loading, an example of which is shown in Fig. 3c [34,48]. We should note that the present test specimen geometry has an inherent limitation for fracture toughness determination in that it promotes crack-tip blunting due to the steep stress/strain gradient imposed by a neutral axis located typically only ≈ 150 μm ahead of the crack tip. In fact, in hindsight rather than relying on the bend test geometry, fracture toughness testing for through-thickness crack growth within sheet specimens of high toughness probably should have been performed using an in-plane tension specimen geometry. In any event, for these particular tests, it was impossible to define a J-integral at
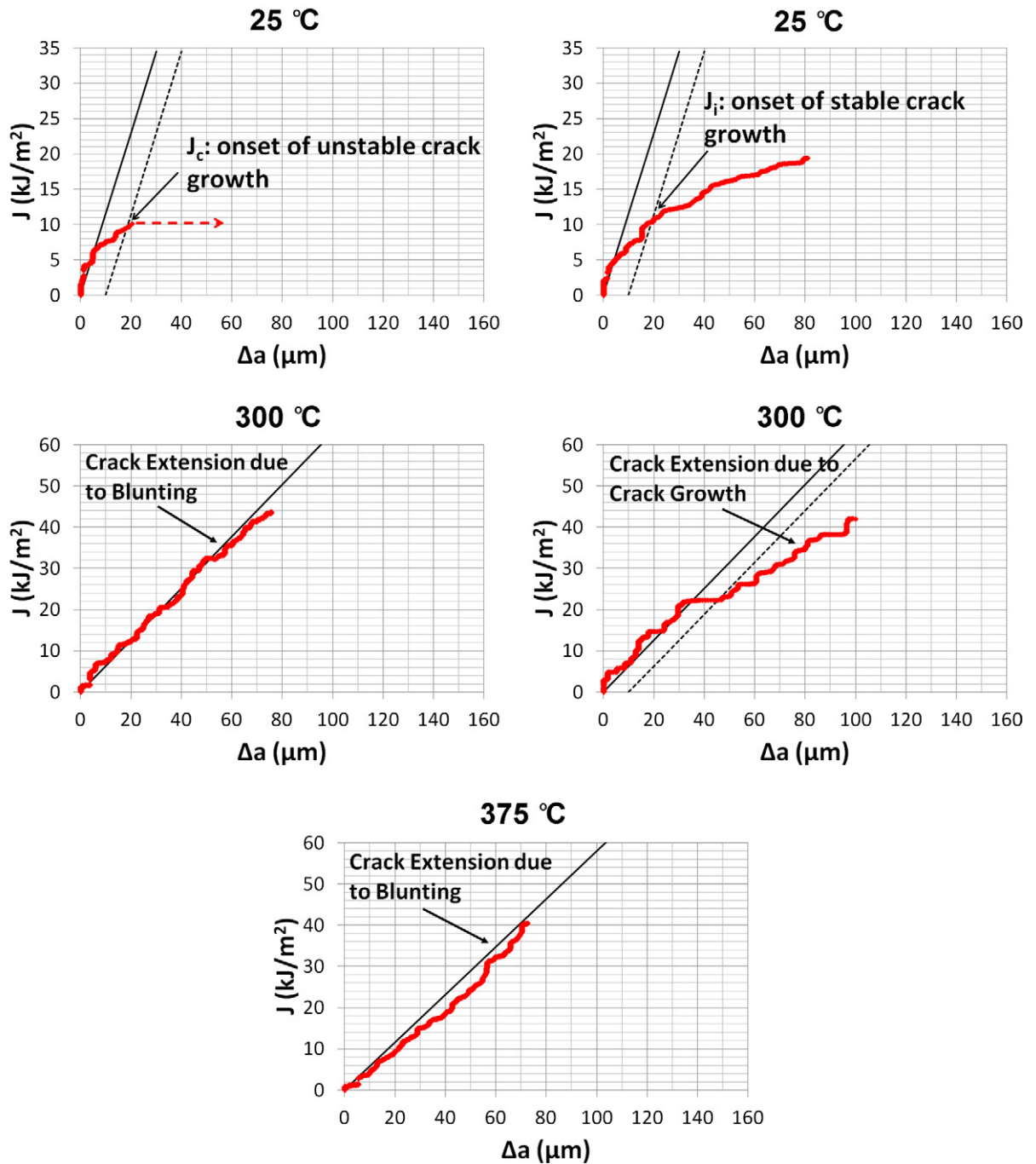
Fig. 13. Examples of *J*–*R* crack-growth resistance behavior observed at 25 °C, 300 °C, and 375 °C.

the onset of crack growth, hence only the *J*-integral at maximum load (J_{Pmax}) was calculated. As a result, the value of J_{Pmax} should be considered a lower bound for the fracture toughness. For this particular *J*–*R* response, the near-linear *J*–*R* behavior continues beyond the magnitude of crack extension (in the range of 40–50 µm) that defines J_{Pmax}, implying a toughness exceeding J_{Pmax}.

3.4. Fracture toughness: the influence of hydrogen and temperature

Both the test temperature and the presence of hydrogen in the Zircaloy-4 matrix are expected to influence fracture toughness. Based on hydrogen contents and hydride microstructures near the crack tip, Fig. 14 shows the fracture toughness (in terms of K_J, in MPa$\sqrt{\text{m}}$, as derived from the *J*-integral using Eq. (5)) as a

function of (a) hydrogen content, and of (b) radial hydride fraction at 25 °C. We should note that the higher values of radial hydride fraction shown in Fig. 14 were obtained for sheet specimens tested in uniaxial tension (rather than bending) and refer to crack propagation in the "sunburst" region near the blister. It should be noted that at 25 °C, due to higher hydrogen contents and higher radial hydride fractions near the hydride blister, crack growth occurred first along the crack front where the crack depth was the smallest, and therefore at a location where the local stress intensity factor was lowest (see Fig. 7a discussion). This effect caused the crack depth to become more uniform as it propagated. In calculating the fracture toughness for crack growth initiation, the crack-front was taken into account and Franc3D analysis showed that for some specimens, the effective stress intensity roughly corresponded to
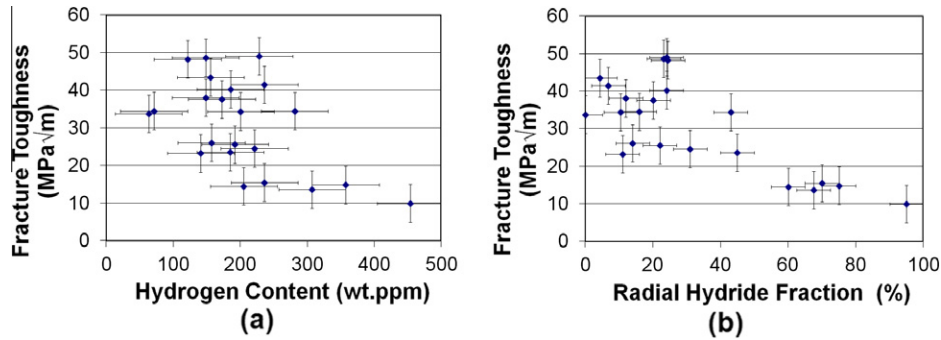
Fig. 14. Fracture toughness as a function of (a) hydrogen content (as measured in the substrate by area fraction analysis), and (b) radial hydride fraction for specimens tested at 25 °C. The error bars for fracture toughness are estimated at ±5 MPa√m based on sensitivity of the electrical potential drop equipment. The error bars for hydrogen content and for radial hydride fraction are estimated at ±50 wt.ppm and ±5%, respectively, based on the sensitivity of the image analysis results to image contrast and etching effects.

values as low as ∼85–90% of the toughness calculated using the average crack length provided by EPD measurement. Finally, a comparison of room temperature fracture toughness data obtained from tests in which only blister pre-cracking was used [27,28] with those obtained from fatigue pre-cracked specimen showed similar fracture toughness values for similar hydride microstructures at a given temperature.

Inspection of Fig. 14a shows that at 25 °C the fracture toughness values decrease from ∼45 MPa√m for hydrogen contents lower than 200 wt.ppm to 10–15 MPa√m for hydrogen contents in excess of 300 wt.ppm. Specifically, there appears to be a significant drop in toughness values for hydrogen contents above ∼200 wt.ppm. Furthermore, as would be expected, Fig. 14b shows that the toughness values at a given hydrogen content also decrease with increasing radial hydride fraction (RHF). For the case of crack growth into sunburst hydrides (where previous microstructures have been re-analyzed), the result show that for RHF > 60%, the fracture toughness values decline to the range of 10–15 MPa√m. We should caution that since the same samples that exhibit high hydrogen content also exhibit high radial hydride fractions, our study does not separate the two effects. As shown in Fig. 15a, the higher RHF resulted in a fracture surface characterized by shallow dimples, tear ridges, and a relatively flat fracture surface, consistent with a low energy fracture process. In contrast, Fig. 15b indicates that a low RHF resulted in the formation of large elongated primary voids (induced by circumferential hydrides) that caused crack deflection and crack-tip blunting, thus increasing the crack growth resistance relative to that observed for microstructures with a higher RHF.

The decrease of fracture toughness with increasing hydrogen content at room temperature agrees with previous studies on zirconium-based alloys [6–8,13,15–17]. The decreased fracture

toughness for higher RHF at room temperature is also similar to what was reported by Honda [9], Chow and Simpson [54], Davies and Stearns [11] and Bertolino et al. [16] in previous studies of axial crack growth in plate made of Zr–2.5%Nb, Zircaloy-2 or Zircaloy-4, respectively. Furthermore, the fracture toughness values found here for low hydrogen contents (∼35–45 MPa√m for [H] ∼ 50 wt.ppm) are in good agreement with those found by Walker and Kass for through-thickness crack growth in thick Zircaloy-4 plate (≈35–40 MPa√m) [23,24], but they are lower than those found by Grigoriev and Jakobsson [14] and Bertsch and Hoffelner [19] for axial crack growth in thin-wall Zircaloy-4 cladding (∼90–100 MPa√m). This factor of ∼2–3 difference between the fracture toughness for axial and through-thickness crack growth in thin-wall material is consistent with the high toughness levels typically observed when the lack of through-thickness crack-tip constraint results in mode I + III crack growth in axial crack growth. In the present study, mode I crack growth was observed at room temperature, and it occurred under conditions of plane-strain along the crack tip (even though the material is thin sheet). The result is a higher degree of constraint at the crack-tip for through-thickness crack growth than for axial crack growth, resulting in lower fracture toughness in these thin sheet bend tests.

The through-thickness fracture toughness data in Fig. 16 offer limited interpretation. In contrast to the room temperature toughness behavior, the elevated temperature J–R data presented earlier show two types of crack extension behavior, and the corresponding toughness data are presented in Fig. 16. At 300 °C and especially at 375 °C, it will be recalled that crack extension in some tests can be caused solely by what appears to be crack-tip blunting—even well past maximum load when the specimen is quite bent. For these crack-tip blunting cases, the values of K_{JPmax} (based on maximum load) are presented as a lower bound for the fracture toughness
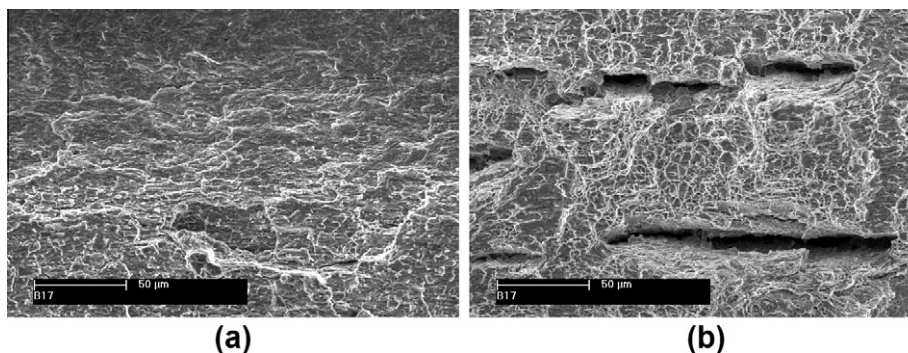

Fig. 15. SEM fractographs for a specimen tested at 25 °C, for crack growth into (a) the sunburst hydride region, and (b) the circumferential hydride region.
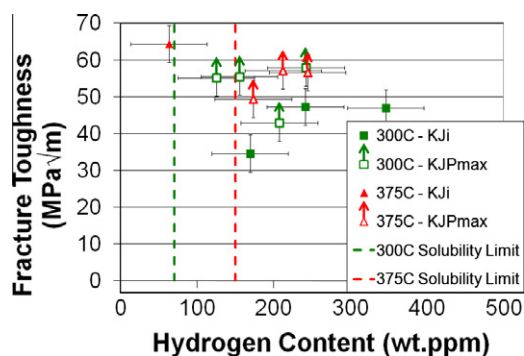
Fig. 16. The fracture toughness (K_{Ji}) or the lower bound estimate of fracture toughness based on maximum load ($K_{JP\text{max}}$) as a function of hydrogen contents at either 300 °C or 375 °C.

at the onset of crack growth (upward pointing arrows). On the other hand, in some of the elevated temperature tests (three of seven tests at 300 °C and one test at 375 °C), the J–R data indicated crack growth initiation occurred after a short period of crack-tip blunting, and Fig. 16 shows the corresponding K_{Ji}-values.

In view of the above elevated temperature crack-extension responses observed, with the exception of one 300 °C test result the fracture toughness values at the two elevated temperatures are greater than those shown in Fig. 15 at room temperature, as would be expected. In addition, the data suggest that the fracture toughness may be somewhat higher at 375 °C than at 300 °C. Based on the $K_{JP\text{max}}$-values as lower limits, the limited results in Fig. 16 indicate that the fracture toughness for through-thickness crack growth is roughly $\geqslant 55$ MPa$\sqrt{}$m at 300 °C and >55 MPa$\sqrt{}$m at 375 °C. At both of these elevated temperatures, the toughness-values do not appear to depend on hydrogen content, even after the solubility of hydrogen at temperature is taken into account. [It should be noted that the hydrogen solubility in Zircaloy-4 is 70 wt.ppm and 150 wt.ppm at 300 °C and 375 °C, respectively [41]. As estimated from metallography near the crack tips, the hydrogen contents of all but one of the specimens tested would still imply that at least some hydride particles are precipitated within the Zircaloy-4 matrix at these temperatures.]

The above toughness values ($\geqslant 50$ MPa$\sqrt{}$m at 300 °C and >55 MPa$\sqrt{}$m at 375 °C) are consistent with those found by Honda for through-thickness crack growth in Zr–2.5Nb thick-tube specimens ($K_c \sim 60$ MPa$\sqrt{}$m at 300 °C) [9], but they are much lower than that found by Davies et al. for *axial* crack growth in Zircaloy-2 thick-wall tube ($K_{JP\text{max}} \sim 150$ MPa$\sqrt{}$m at 300 °C) [11]. Also for axial crack growth in Zircaloy-4 thin-wall cladding tube at 300 °C, Grigoriev and Jakobsson [14] and Hsu [18] found that $K_{JP\text{max}} \sim 89$ MPa$\sqrt{}$m, while Ste.-Catherine found that the toughness exceeded 150 MPa$\sqrt{}$m [20]. As previously discussed, mode I + III axial crack growth in thin wall cladding is expected to be characterized by significantly higher toughness values than those found in this study for through-thickness crack growth. Finally, all of the above studies also found that hydrogen content had little or no influence on fracture toughness at 300 °C, even for hydrogen contents as high as 900 wt.ppm.

The contrast in crack extension behavior at 300 °C and 375 °C with that at 25 °C is likely related to the influence of temperature on the fracture behavior of hydride Zircaloy-4. At 25 °C, the hydride particles directly promote crack growth and fracture. The fractured hydride particles initiate damage accumulation at/or near the crack tip, and play a dominant role in the fracture process. The SEM observations of the fracture surfaces at 300 °C and 375 °C suggest that the hydrides do not participate directly damage accumulation at the crack tip even though (given their hydrogen contents) hydrides should exist within the material at these temperatures

(see Fig. 16). This is consistent with other elevated temperature studies involving fracture of hydrogen-charged Zircaloy-4 [27,34,46,55]. As a result, the fracture surfaces formed during elevated temperature testing are characterized by equiaxed dimples and by the *absence* of hydride-induced primary voids. Similarly, no hydride-induced damage ahead of the crack tip was observed when examining crack tip profiles at these elevated temperatures, as shown in Fig. 6. These observations are in agreement with studies by Simpson [10] and by Davies and Stearns [11] that showed that even in the presence of radial hydrides, the influence of hydrogen on fracture toughness essentially disappears above 300 °C.

Finally, we speculate that the resistance to the growth of a through-thickness crack in a thin wall zirconium alloy component at elevated temperatures may be sufficiently high so that an alternate mode of fracture may dominate. Under the plane-strain deformation condition near a blunted crack-tip, failure due to a through-thickness deformation localization process is a distinct possibility.

4. Conclusions

The fracture toughness behavior of unirradiated hydrided cold worked stress relieved Zircaloy-4 sheet was investigated under conditions of through-thickness crack growth at 25 °C, 300 °C, and 375 °C as a function of hydrogen content and hydride orientation at 25 °C. A linear hydride blister was used to initiate a through-thickness crack across a thin sheet specimen, which was extended using fatigue pre-cracking. Subsequent crack extension was monitored during tensile loading such that crack extension resistance could be determined. Crack-front profiles across the specimen width were experimentally determined, and Franc3D modeling was performed to take into account non-uniform crack fronts. Elastic–plastic fracture mechanics analyses were extended by performing finite element analyses with Cast3M to address crack growth in thin-sheet geometries. The resulting load–displacement and crack-growth data could then be analyzed to obtain J–R curves for elastic–plastic crack growth in this specimen geometry.

The hydride microstructures within the Zircaloy-4 sheet were characterized by a through-thickness gradient in the hydrogen content and in the hydride orientation, such that the hydrogen concentration and (at least at room temperature) the radial hydride fraction increased near the hydride blister. Image analysis techniques were employed to estimate both the radial hydride fraction and the hydrogen content on a local basis such that near crack-tip values could be established.

The main results of this study are:

1. Analysis of J–R curves showed that through-thickness crack growth extension at 25 °C decreased from ~ 45 MPa$\sqrt{}$m to 10–15 MPa$\sqrt{}$m with increasing hydrogen content and radial hydride fraction. Specifically, there appeared to be a significant drop in toughness values for hydrogen contents above ~ 200 wt.ppm H. In addition, low toughnesses occur at radial hydride fractions above 60%. Crack-tip profiles and fractography indicated that the crack growth process at 25 °C followed the radial hydrides when these were present at the crack tip. When the crack tip encounters in-plane hydrides, the crack growth process was initiated by the formation of primary voids at fractured hydride particles, and crack growth occurred by linking the crack tip with the next hydride-induced void ahead of it.

2. At 300 °C and 375 °C, the crack extension observed in bend tests of the pre-cracked (thin) sheet specimens could often be attributed to crack-tip blunting (even well past maximum load) instead of crack growth initiation. In these cases, the toughness values resulting from an analysis of the J–R behavior was inter-

preted as the *lower bound* values for the fracture toughness. Combining these lower bound values with those few toughness-values where crack growth initiation was established indicates approximate fracture toughness-values of $\geqslant 50$ MPa$\sqrt{m}$ at 300 °C and >55 MPa$\sqrt{m}$ at 375 °C. At these temperatures the hydrogen content had no apparent influence on the associated fracture toughness values, up to values of 250 and 350 wt.ppm, respectively. This conclusion was supported by fractographic evidence that indicated hydride particles did not initiate damage such as primary voids.

Acknowledgments

References

[1] R. Yang, O. Ozer, H. Rosenbaum, Current Challenges and Expectations of High Performance Fuel for the Millenium, Light Water Reactor Fuel Performance Meeting, Park City, Utah, ANS, 2000.
[2] J. Papin, B. Cazalis, J.M. Frizonnet, J. Desquines, F. Lemoine, V. Georgenthum, F. Lamare, M. Petit, Nucl. Technol. 157 (2007) 230–250.
[3] A.M. Garde, G.P. Smith, R.C. Pirek, Effects of hydride precipitate localization and neutron fluence on the ductility of irradiated Zircaloy-4, in: E.R. Bradley, G.P. Sabol (Eds.), Zirconium in the Nuclear Industry: 11th International Symposium, STP vol. 1295, ASTM, West Conshohocken, PA, 1996, pp. 407–430.
[4] R.O. Meyer, An Assessment of Fuel Damage in Postulated Reactivity-Initiated Accidents, Report ML0521704030, US Nuclear Regulatory Commission, Washington, DC, 2005.
[5] R.S. Daum, S. Majumdar, D.W. Bates, A.T. Motta, D.A. Koss, M.C. Billone, On the embrittlement of Zircaloy-4 under RIA-relevant conditions, in: G.D. Moan, P. Rudling (Eds.), Zirconium in the Nuclear Industry: 13th International Symposium, STP vol. 1423, ASTM, West Conshohocken, PA, 2002, pp. 702–719.
[6] R.G. Hoagland, R.G. Rowe, J. Nucl. Mater. 30 (1–2) (1969) 179–195.
[7] I. Aitchison, The effect of orientation of hydride precipitates on the fracture toughness of cold-rolled Zircaloy-2 and 2.5Nb zirconium, in: Applications-Related Phenomena for Zirconium and its Alloys, STP vol. 458, ASTM, Philadelphia, PA, 1969, pp. 160–178.
[8] B. Watkins, A. Cowan, G.W. Parry, B.W. Pickles, Embrittlement of Zircaloy-2 pressure tubes, in: Applications-Related Phenomena for Zirconium and Its Alloys, STP vol. 458, ASTM, Philadelphia, PA, 1969, pp. 141–159.
[9] S.-I. Honda, Nucl. Eng. Des. 81 (2) (1984) 159–167.
[10] L.A. Simpson, C.K. Chow, Effect of metallurgical variables and temperature on the fracture toughness of zirconium alloy pressure tubes, in: R.B. Adamson, L.F.P. VanSwam (Eds.), Zirconium in the Nuclear Industry: 7th International Symposium, STP vol. 939, ASTM, Philadelphia, PA, 1987, pp. 579–596.
[11] P.H. Davies, C.P. Stearns, Fracture toughness testing of Zircaloy-2 pressure tube material with radial hydrides using direct-current potential drop, in: J.H. Underwood, R. Chait (Eds.), Fracture Mechanics: 17th Volume, STP vol. 905, ASTM, Philadelphia, PA, 1986, pp. 379–400.
[12] F.H. Huang, Fracture toughness evaluation for Zircaloy-2 pressure tubes with the electric-potential method, in: W.R. Corwin, F.M. Haggag, W.L. Server (Eds.), Small Specimen Techniques Applied to Nuclear Reactor Vessel Thermal Annealing and Plant Life Extension, STP vol. 1204, ASTM, Philadelphia, PA, 1993, pp. 182–198.
[13] J.S. Dubey, S.L. Wadekar, R.N. Singh, T.K. Sinha, J.K. Chakravartty, J. Nucl. Mater. 264 (1–2) (1998) 20–28.
[14] V. Grigoriev, R. Jakobsson, J. ASTM Int. 2 (8) (2005) 16–31.
[15] G. Bertolino, G. Meyer, J. Perez-Ipina, J. Nucl. Mater. 320 (2003) 272–279.
[16] G. Bertolino, J. Perez-Ipina, G. Meyer, J. Nucl. Mater. 322 (2003) 57–65.
[17] G. Bertolino, J. Perez-Ipina, G. Meyer, J. Nucl. Mater. 348 (1–2) (2006) 205–212.
[18] H.H. Hsu, J. Alloys Compd. 426 (1–2) (2006) 256–262.
[19] J. Bertsch, W. Hoffelner, J. Nucl. Mater. 352 (1–3) (2006) 116–125.
[20] C. Ste.-Catherine, D. Le Boulch, S. Carassou, N. Ramasubramanian, C. Lemaignan, J. Test. Eval. 34 (5) (2006).
[21] P.H. Kreyns, W.F. Bourgeois, C.J. White, P.L. Carpenter, B.F. Kammenzind, D.G. Franklin, Embrittlement of reactor core materials, in: E.R. Bradley, G.P. Sabol (Eds.), Zirconium in the Nuclear Industry: 11th International Symposium, STP vol. 1295, ASTM, West Conshohocken, PA, 1996, pp. 758–781.
[22] B.V. Cockeram, K.S. Chan, J. Nucl. Mater. 393 (2009) 387–408.
[23] T.J. Walker, Nucl. Technol. 16 (3) (1972) 509–520.
[24] T.J. Walker, J.N. Kass, Variation of Zircaloy fracture toughness in irradiation, in: Zirconium in Nuclear Applications, STP vol. 551, ASTM, Philadelphia, PA, 1974, pp. 328–354.
[25] P.H. Davies, J.M. Smeltzer, J-controlled crack growth (size effects) in fracture toughness testing of Zr–2.5%Nb pressure tube material, in: H.A. Ernst, A. Saxena, D.L. McDowell (Eds.), Fracture Mechanics: 22nd Symposium (1), STP vol. 1131, ASTM, Philadelphia, PA, 1992, pp. 93–104.
[26] V. Grigoriev, B. Josefsson, A. Lind, B. Rosborg, Scripta Metall. Mater. 33 (1) (1995) 109–114.
[27] P.A. Raynaud, D.A. Koss, A.T. Motta, K.S. Chan, J. ASTM Int. 5 (1) (2007).
[28] P.A. Raynaud, D.A. Koss, A.T. Motta, K.S. Chan, Fracture of hydrided Zircaloy-4 sheet under through-thickness crack growth conditions, in: Proceedings of International LWR Fuel Performance Meeting, San Francisco, CA, September 30th–October 3rd, 2007.
[29] P.A. Raynaud, M.J. Meholic, D.A. Koss, A.T. Motta, K.S. Chan, Influence of hydride microstructure on through-thickness crack growth in Zircaloy-4 sheet, in: 13th International Conference on Environmental Degradation of Materials in Nuclear Power Systems, Whistler, BC, 2007.
[30] Standard Test Method for Measurement of Fracture Toughness, Standard Practice E1820-08, ASTM, West Conshohocken, PA, 2008.
[31] T.M. Link, D.A. Koss, A.T. Motta, Nucl. Eng. Des. 186 (3) (1998) 379–394.
[32] J.J. Kearns, C.R. Woods, J. Nucl. Mater. 20 (3) (1966) 241–261.
[33] J.E. Lewis, G. Schoenberger, R.B. Adamson, Texture measurement techniques for Zircaloy cladding: a round-robin study, in: D.G. Franklin (Ed.), Zirconium in the Nuclear Industry: Fifth Conference, STP vol. 754, ASTM, Philadelphia, PA, 1982, pp. 39–62.
[34] O.N. Pierron, D.A. Koss, A.T. Motta, K.S. Chan, J. Nucl. Mater. 322 (1) (2003) 21–35.
[35] P. Delobelle, P. Robinet, P. Bouffioux, P. Greyer, I. LePichon, A unified model to describe the anisotropic viscoplastic Zircaloy-4 cladding tubes, in: E.R. Bradley, G.P. Sabol (Eds.), Zirconium in the Nuclear Industry: 11th International Symposium, STP vol. 1295, ASTM, West Conshohocken, PA, 1996, pp. 373–393.
[36] J. Desquines, B. Cazalis, C. Bernaudat, C. Poussard, X. Averty, P. Yvon, J. ASTM Int. 2 (6) (2005).
[37] H.H. Johnson, Mater. Res. Stand. 5 (9) (1965) 442–445.
[38] Cornell Fracture Group, 2008. <http://www.cfg.cornell.edu/index.htm>.
[39] T.J. Collins, BioTechniques 43 (2007) 25–30.
[40] F. Nagase, H. Uetsuka, Hydride Morphology and Hydrogen Embrittlement of Zircaloy fuel Cladding used in NSRR/HBO Experiment, ANS International Topical Meeting on Light Water Reactor Performance, Portland, OR, 1997.
[41] R.S. Daum, Hydride-Induced Embrittlement of Zircaloy-4 Cladding under Plane Strain Tension, Ph.D. Thesis in Materials Science and Engineering, Pennsylvania State University, 2007.
[42] J.J. Kearns, J. Nucl. Mater. 22 (3) (1967) 292–303.
[43] A. McMinn, E.C. Darby, J.S. Schofield, The terminal solid solubility of hydrogen in zirconium alloys, in: G.P. Sabol, J. Moan (Eds.), Zirconium in the Nuclear Industry: 12th International Symposium, STP vol. 1354, ASTM, Philadelphia, PA, 2000, pp. 173–195.
[44] P. Raynaud, Crack Growth Through the Thickness of Thin Sheet Hydrided Zircaloy-4, PhD Thesis in Materials Science and Engineering, The Pennsylvania State University, 2009.
[45] Proprietary Code, French Patent # BD10308.
[46] T.L. Anderson, Fracture toughness testing of metals, in: Fracture Mechanics: Fundamentals and Applications, third ed., Taylor & Francis/CRC Press, 2005.
[47] A. Glendening, D.A. Koss, A.T. Motta, R.S. Daum, J. ASTM Int. 2 (2005) 399–414.
[48] O.N. Pierron, Influence of Hydride Blisters on Failure of Zircaloy-4 Sheet, M.S. Thesis in Materials Science and Engineering, The Pennsylvania State University, 2002.
[49] Y.J. Kim, Eng. Fract. Mech. 69 (7) (2002) 793.
[50] J. Sumpter, Fatigue Eng. Mater. Struct. 10 (6) (1987) 479–493.
[51] S.X. Wu, Y.W. Mai, B. Cotterell, Int. J. Fract. 45 (1990) 1–18.
[52] CEA, 2010. <http://www-cast3m.cea.fr/cast3m/index.jsp>.
[53] C.M. Davies, M. Kourmpetis, N.P. O'Dowl, K.M. Nikbin, Experimental evaluation of the J or C* parameter for a range of cracked geometries, in: R.E. Link, K.M. Nikbin (Eds.), Fatigue and Fracture Mechanics, 35th Volume, STP vol. 1480, ASTM, West Conshohocken, PA, 2005, pp. 312–340.
[54] C.K. Chow, L.A. Simpson, Analysis of the unstable fracture of a reactor pressure tube using fracture toughness mapping, in: C.M. Hudson, T.P. Rich (Eds.), Case Histories Involving Fatigue and Fracture Mechanics, STP vol. 918, ASTM, Philadelphia, PA, 1986, pp. 78–101.
[55] M. Le Saux, J. Besson, S. Carassou, C. Poussard, X. Averty, Eng. Fail. Anal. 17 (2010) 683–700.